Model of superconducting vortices in layered materials for the interpretation of transmission electron microscopy images

M. Beleggia,[1] G. Pozzi,[2] A. Tonomura,[3,4,5] H. Kasai,[3,4] T. Matsuda,[5,6] K. Harada,[3,5] T. Akashi,[4,7] T. Masui,[8] and S. Tajima[8]
[1]*Center for Functional Nanomaterials, Brookhaven National Laboratory, Upton, New York 11973, USA*
[2]*Department of Physics and Istituto Nazionale per la Fisica della Materia, University of Bologna, Viale B. Pichat 6/2, 40127 Bologna, Italy*
[3]*Advanced Research Laboratory, Hitachi, Ltd., Hatoyama, Saitama 350-0395, Japan*
[4]*SORST, Japan Science and Technology Corporation (JST), 3-4-15 Nihonbashi, Chuo-ku, Tokyo 103-0027, Japan*
[5]*Frontier Research System, The Institute of Chemical and Physical Research (RIKEN), Wako, Hirosawa, Saitama 351-0198, Japan*
[6]*Hitachi Science Systems, Ltd., 1040 Ichige, Hitachinaka, Ibaraki 312-0033, Japan*
[7]*Hitachi Instruments Service Co., Ltd., 4-28-8 Yotsuya, Shinjuku-ku, Tokyo 160-0004, Japan*
[8]*International Superconductivity Technology Center (ISTEC), Shinonome, Koto-ku, Tokyo 135-0062, Japan*
(Received 6 April 2004; published 18 November 2004)

More realistic simulations of the magnetic field and electron optical phase shift associated to pancake vortices in layered high-T_c superconducting specimen require a number of layers larger than 7, the practical upper limit set by the discrete algebraic approach followed so far. This goal can be achieved by resorting to a continuum approximation of the screening layers above and below the one containing the pancake vortex. It is thus possible to increase the number of layers and to investigate more exotic vortex core structures than those represented by the pancakes pinned at tilted columnar defects. In particular it will be shown how recently observed dumbbell-like contrast features in the out-of-focus images of superconducting vortices forming a large angle with the specimen surfaces can be interpreted as due to a kinked structure of the pancakes.

DOI: 10.1103/PhysRevB.70.184518 PACS number(s): 74.78.Bz, 74.25.Qt, 68.37.Lp, 61.14.Nm

I. INTRODUCTION

Transmission electron microscopy (TEM) techniques, like Lorentz microscopy[1] and electron holography,[2] allow direct observation of individual vortices inside superconducting thin films. Like other methods, e.g., Bitter decoration,[3] scanning tunnel,[4] and scanning electron[5] microscopy, scanning Hall probes,[6] SQUID,[7] magneto-optical techniques,[8] scanning tunnel spectroscopy,[9] and magnetic force microscopy,[10] vortices are imaged under a wide range of experimental conditions. However, while the signal in most of the cited techniques depends on the magnetic field on the surface and in the half-space surrounding the specimen, the contrast of the TEM images depends also on the core structure, especially when experiments are carried out with the newly developed 1 MV field emission electron microscope,[11] where specimens thicker than 400 nm can be analyzed.

This has been clearly demonstrated in recent TEM observations of vortices interacting with columnar defects in high-T_c superconductors,[12] where peculiar contrast features have been observed. In particular, the images of pinned vortices displayed less contrast than the unpinned ones and this effect has been attributed to the anisotropy of the superconducting material by comparing the experimental results with the theoretical ones, calculated by using both an anisotropic and a layered model.[13,14] However, in this latter case, the number of layers dictated by the algebraic approach followed was limited to seven, a rather small number to be truly representative of the actual specimen where the layers are about 100 to 200. Nonetheless, the contour line maps of the projected magnetic field showed a strong overall similarity with the continuous anisotropic case and also the out-of-focus images calculated for vortex cores pinned at tilted columnar defects showed no significant differences.[14]

Further experiments carried out with applied magnetic field tilted at a very large angle with respect to the specimen surfaces[15] showed new interesting features in the out-of-focus images. By increasing the angle the vortex cores become first elongated as if they were following the direction of the field and then, at the largest angle, sometimes exhibit a dumbbell-like appearance. These observations indicate that something new is happening to the vortex structure. Unfortunately these features cannot be interpreted on the basis of the available models. In fact, in the continuous-anisotropic model the vortex core is straight and aligned with the field, and with the pancake model at such large angles the small number of layers can be detected in the image, introducing unwanted artifacts.

In order to develop a more flexible model, two options are available: deforming the core in the continuous-anisotropic model, or giving suitable coordinates for the location of each pancake in the stack. While the first turns out to be very cumbersome, the second is more practicable, provided the number of layers is increased. For this purpose, we follow the approach proposed by Clem[16,17] and further developed by Coffey and Phipps,[18] who replaced all the screening layers above and below the layer containing the vortex with a superconducting continuum that carries supercurrents parallel to the layers. In this way the algebric troubles linked to the increasing number of unknowns arising in the former approach are circumvented and an analytical expression for the field and phase shift for the single pancake can be obtained. Then, from the solution, more representative or exotic vortex structures can be investigated by adding suitably placed pancakes over a larger number of layers.

After recalling the main conventions for the various reference systems necessary for describing the experimental setup, we show how to find the solution for the vector potential for the case of a pancake vortex embedded in the superconductor slab by Fourier methods. As proposed by Pearl,[20] the boundary condition at the layer containing the pancake vortex can be found by averaging the London equation across the layer. In this way, a relation between the core London singularity and the normal derivatives of the potential above and below the layer is obtained.[14] It can be ascertained that our solution coincides with that found by Coffey and Phipps,[18] when the leading terms with respect to the layer thickness are retained. This result can also be confirmed by a more conventional approach, where the solution of the vector potential for a vortex lying in a thin slice embedded in the superconductor is found and the limit for vanishing thickness of the slice taken afterwards.

Once the solution of the vector potential in the whole space has been found, the electron optical phase shift is calculated by integrating it along a straight trajectory suitably chosen in order to take correctly into account the overall geometry of the experimental setup, including a tilt of the specimen with respect to the electron beam.[13,14] The averaged field in other directions, useful for displaying its main features, is calculated according to the same recipe. Finally, the Kirchhoff-Fresnel diffraction integral is used for the calculations of the out-of-focus images assuming various configurations for the pancake cores, showing that the dumbbell contrast is in agreement with a kinked structure of the vortex.

II. GENERAL CONSIDERATIONS

Let us first recall the main conventions regarding the coordinate systems and the basic formulas describing the interaction of the electron beam with the magnetic field associated to a pancake vortex centered in (x_P, y_P, z_P). Two coordinate systems have been introduced and described,[14,21] namely, (i) the microscope coordinate system having the z axis parallel to the electron beam and aligned in the same direction, with (x,y) being the coordinates in the object plane, perpendicular to the optical axis z, and (ii) the specimen reference system (x_S, y_S, z_S), having its z_S axis, of unit vector $\mathbf{k}_S$, coincident with the specimen normal $\mathbf{n}$ and oriented in the opposite direction as z, the x_S axis, of unit vector $\mathbf{i}_S$, having initially the same direction as x, and the y_S axis determined by the requirement of left handedness, i.e., opposite to y.

The specimen, assumed of constant thickness $t=2d$, can be inclined on an angle α with respect to the electron beam, around the tilt axis coincident with the y (and y_S) axis. The specimen can be also rotated on an azimuth angle β around its normal $\mathbf{n}$, coincident with the tilted z_S axis. A sketch of the specimen reference system, with the pancake layer embedded in the continuum superconducting slab is shown in Fig. 1.

In order to describe the interaction between the electron beam and the magnetic field associated to the vortex, the standard high-energy or phase object approximation is used, according to which the vortex is a pure phase object,[22,23] with the magnetic phase shift given by

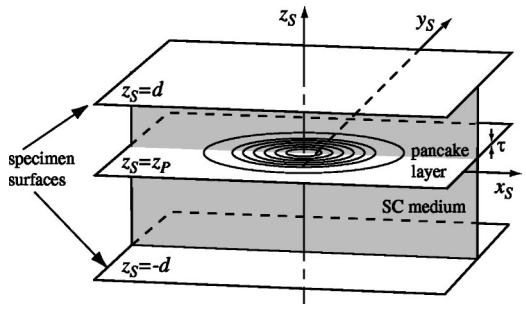

FIG. 1. Scheme of the reference system and of the pancake layer (of small thickness τ) positioned at $z_S=z_P$ and surrounded by a superconducting continuum.

$$\varphi(x,y) = -\frac{2\pi e}{h}\int_{\ell}\mathbf{A}\cdot d\ell = -\frac{\pi}{\phi_0}\int_{-\infty}^{+\infty}A_z(x,y,z)dz, \quad (1)$$

where $\mathbf{A}$ is the vector potential, e and h are the absolute value of the electron charge and the Planck constant, respectively, $\phi_0=h/2e$ is the flux quantum, and x and y are kept fixed since we consider an electron trajectory parallel and in the same direction as the z axis.

This trajectory passes through the regions above, within and below the specimen, thus crossing three separated space domains. For the calculation of the phase shift by means of Eq. (1), in order to avoid unwanted extra terms arising from contour integrals on the domain boundary, it is essential to choose a vector potential continuous in its components parallel to the boundaries.[21]

In the specimen system, the above trajectory is characterized by the parametric equation

$$\ell = (x_S - w\tan\alpha\cos\beta)\mathbf{i}_S + (y_S - w\tan\alpha\sin\beta)\mathbf{j}_S + w\mathbf{k}_S, \quad (2)$$

where w ranges between $(+\infty,-\infty)$ due to the fact that $\mathbf{k}_S$ and $\mathbf{k}$ point in opposite directions. The correspondence between the coordinates of the intersection of the trajectory with the object plane (x,y) and with the specimen midplane (x_S,y_S) is given by

$$x_S = x\frac{\cos\beta}{\cos\alpha} + y\sin\beta, \quad y_S = x\frac{\sin\beta}{\cos\alpha} - y\cos\beta. \quad (3)$$

Therefore, the phase shift Eq. (1) can be calculated in the specimen system according to the relation

$$\varphi(x_S,y_S) = \frac{e}{\hbar}\int_{+\infty}^{-\infty}\mathbf{A}(x_S - w\tan\alpha\cos\beta, y_S - w\tan\alpha\sin\beta, w)\cdot\begin{pmatrix}\tan\alpha\cos\beta\\ \tan\alpha\sin\beta\\ -1\end{pmatrix}dw. \quad (4)$$

and converted finally in the microscope reference system through the indicated coordinate transformations.

Once the object phase $\varphi(x,y)$ is calculated for a specimen tilted at an angle α, and rotated by an azimuth angle β, it may be displayed by means of amplified contour maps, where the intensity $I(x,y)$ is given by

$$I(x,y) = 1 + \cos[n\varphi(x,y)] \tag{5}$$

with n the amplification factor. These phase maps mimic the result of an ideal holographic reconstruction.

As regards the Fresnel phase contrast method, starting from the object phase the out-of-focus images in the observation plane, located at a distance Z from the object plane, can be calculated by means of the Kirchhoff-Fresnel integral,[24]

$$I(X,Y,Z) = \left| \frac{1}{\lambda_e Z} \int\int e^{i\varphi(x,y)} e^{(i\pi/\lambda_e Z)[(x-X)^2+(y-Y)^2]}\, dx\, dy \right|^2, \tag{6}$$

where X and Y are the coordinates in the out-of-focus plane, and λ_e is the de Broglie wavelength of the incident electrons.

III. PANCAKE VORTEX IN A THIN SLAB

In this section we basically follow the approach introduced by Clem[16,17] and Coffey and Phipps,[18] with the difference that the emphasis is put on the vector potential, which is the basic quantity for the calculation of the electron optical phase shift, and not on the magnetic field. Let us consider a London vortex with its core and its magnetic flux aligned along $\mathbf{k}_S$ lying in a thin slice, of negligible thickness τ located at $z=z_P$ (see Fig. 1). Within the slice the vector potential satisfies the modified London equation

$$\mathbf{A} - \lambda^2 \nabla^2 \mathbf{A} = -\frac{\phi_0}{2\pi} \frac{\mathbf{r}_S \times \mathbf{k}_S}{r_S^2} \equiv \mathbf{\Phi}_L, \tag{7}$$

where $\lambda = \lambda_{ab}$ is the penetration depth in the ab plane, $\mathbf{r}_S$ represents a two-dimensional position vector perpendicular to the direction $\mathbf{k}_S$ of the core and $\mathbf{\Phi}_L$ is defined as the London vector.

By averaging the modified London equation over the layer thickness the following "jump" condition results:[18,19]

$$\mathbf{A}(x_S,y_S,z_P) - \Lambda \left\{ \left[\frac{\partial \mathbf{A}}{\partial z_S} \right]_{z_P^+} - \left[\frac{\partial \mathbf{A}}{\partial z_S} \right]_{z_P^-} \right\} = \mathbf{\Phi}_L, \tag{8}$$

where $\Lambda = \lambda^2/\tau$ is the Pearl film penetration depth. Equation (8) relates the normal derivatives of the vector potential at the upper ($z=z_P^+$) and lower ($z=z_P^-$) surfaces with its average value and the London vector.

In the rest of the superconducting slab, the vector potential satisfies the homogeneous London equation,

$$\mathbf{A} - \lambda^2 \nabla^2 \mathbf{A} = 0, \tag{9}$$

whereas in the vacuum regions above and below the specimen the Laplace equation,

$$\nabla^2 \mathbf{A} = 0. \tag{10}$$

This problem can be analyzed and solved by two-dimensional Fourier methods, as suggested by the presence of flat boundaries parallel to the (x_S,y_S) plane (see Refs. 14, 18, and 21). In this way, since both the London (for the superconductor) and the Laplace (for the external space) equations are of the second order, the dependence on the third z coordinate contains simple exponential functions.

TABLE I. Simplified structure of the solutions for vector potential (middle column) in the different regions of the specimen. Each region is labeled on the left-hand side (SC stands for superconductor) and corresponds to the intervals of the z axis indicated on the right-hand side. The pancake vortex is located in the layer at $z=z_P$, between regions A_2 and A_3.

A_4: Upper vacuum	$a_4^- e^{-kz}$	$z > d$
A_3: Upper SC	$a_3^+ e^{qz} + a_3^- e^{-qz}$	$z_P < z < d$
A_2: Lower SC	$a_2^+ e^{qz} + a_2^- e^{-qz}$	$-d < z < z_P$
A_1: Lower vacuum	$a_1^+ e^{kz}$	$z < -d$

Following the arguments developed and explained in Refs. 14 and 21 we can express the general solutions for the vector potential in the specimen regions, each satisfying the appropriate differential equation, by

$$\tilde{\mathbf{A}}_j(k_x,k_y,z) = (a_j^+ e^{k_j z} + a_j^- e^{-k_j z}) \tilde{\mathbf{\Phi}}_L, \tag{11}$$

where $\tilde{\mathbf{\Phi}}_L$ is the Fourier transform of the London vector for $\mathbf{k}_S=(0,0,1)$,

$$\tilde{\mathbf{\Phi}}_L = \frac{i\phi_0}{k_x^2 + k_y^2} [k_y, -k_x, 0] \tag{12}$$

which keeps the information on the purely angular dependence of the vector potential (which, if expressed in cylindrical coordinates, would possess only the θ component) as well as the correct dimensionality, in such a way that the a_j are dimensionless coefficients. Moreover, we have $k_j = k \equiv \sqrt{k_x^2 + k_y^2}$ for the vacuum regions and $k_j = q \equiv \sqrt{\lambda^{-2} + k_x^2 + k_y^2}$ for the superconducting regions. Incidentally, we note that the fingerprint of vacuum region is an infinite penetration depth ($q \to k$ for $\lambda \to \infty$).

Once this general description is given, all is left is the determination of the unknown coefficients corresponding to each region. The structure of the vector potential in this formalism, where the common factor $\tilde{\mathbf{\Phi}}_L$ is removed, is sketched in Table I.

The problem is then reduced to the algebraic determination of the coefficients a_j of these exponentials. This can be achieved solving the system obtained by imposing the following boundary conditions: (i) continuity of the vector potential and of its normal derivative at the specimen surfaces $z = \pm d$, (ii) continuity of the vector potential and "jump" condition, i.e., the Fourier-space equivalent of Eq. (8), at the pancake layer $z=z_P$. As a result of the procedure outlined, we obtain the following expression for the vector potential in the various regions,

$$a_4^- = \frac{\tau}{\Delta} e^{kd} \{ q \cosh[q(d+z_P)] + k \sinh[q(d+z_P)] \}, \tag{13}$$

$$a_3^{\pm} = \tau \frac{q \mp k}{2q\Delta} e^{\mp qd}\{q \cosh[q(d + z_P)] + k \sinh[q(d + z_P)]\}, \tag{14}$$

$$a_2^{\pm} = \tau \frac{q \pm k}{2q\Delta} e^{\pm qd}\{q \cosh[q(d - z_P)] + k \sinh[q(d - z_P)]\}, \tag{15}$$

$$a_1^{+} = \frac{\tau}{\Delta} e^{kd}\{q \cosh[q(d - z_P)] + k \sinh[q(d - z_P)]\}, \tag{16}$$

where the common factor Δ is

$$\Delta = (1 + 2k^2\lambda^2)\sinh(qt) + 2kq\lambda^2 \cosh(qt) + B\tau \tag{17}$$

with

$$B = \frac{1}{2q\lambda^2}[(1 + 2\lambda^2 k^2)\cosh(qt) + 2kq\lambda^2 \sinh(qt) + \cosh(2qz_p)]. \tag{18}$$

Even though obtained with different methods and notations, it can be ascertained that the results for the vector potential in Eqs. (13)–(16) coincide with those reported by Coffey and Phipps[18] at the first order in τ, i.e., provided the term containing the slice thickness $B\tau$ in Eq. (17) is neglected. This is justified since the pancake layer can be as thin as a few angstroms. However, in our simulations we have to limit the number of layers to a finite value n_L of the order of 10 or 20. Also in this case, where for a given specimen thickness t we define the pancake layer thickness as $\tau = t/n_L$, we can overlook the additional term.

In order to gain more confidence, we have verified these results employing a different procedure, i.e., solving the problem for a slice of finite thickness. In this approach we have a sytem of eight unknowns, with the boundary conditions of continuity of the vector potential and its normal derivative at the various interfaces. Taking the limit of the resulting solution for vanishing thickness of the slice containing the pancake vortex, we recover the former results with $B\tau$ neglected. This confirms the soundness and the underlying physical foundation of the procedure employed.

Having the solution for a single pancake vortex located at $(0,0,z_P)$, we can describe another vortex, located at (x_P,y_P,z_P), by multiplying its Fourier transform by the factor $e^{-i(x_P k_x + y_P k_y)}$. By superposition, we can finally find the vector potential and the phase shift for an arbitrary arrangement of pancakes.

IV. COMPARISON BETWEEN THE MODELS

It is worthwhile to compare the results obtained by this semicontinuous approach with those of the previous one.[14] First we present the phase maps corresponding to an ideal experiment where the beam direction is parallel to one of the coordinate system axis and the infinite thickness of the specimen is overlooked. Such maps are interpretable as projected magnetic induction maps and give a vivid representation of the trend of the magnetic flux lines piercing the specimen. In the case of a phase map calculated along the y_S axis the following expression will be employed:

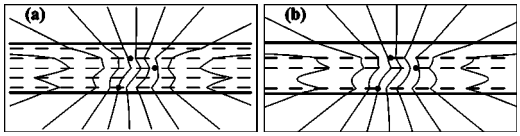

FIG. 2. Contour line plots representing the phase shift calculated with the pancake (a) and semicontinuous (b) models in the y_S direction. The contour lines represent phase shifts of 200 mrad. Simulation parameters, plot region 2×1 μm, specimen thickness t = 400 nm and λ = 200 nm. The dots mark the positions of the pancake vortices.

$$\phi(x_S,z_S) = \frac{i}{\phi_0}\int_0^{\infty} \tilde{A}_y(k_x,0,z_S)\sin(x_S k_x)dk_x. \tag{19}$$

Figure 2 shows the comparison between the calculations carried out for three pancake layers (whose core is marked by a thick dot) in the case of a finite layered structure composed of five layers (a) and within the new semicontinuous model (b). The overall similarity between the two cases is clearly displayed, with small differences detectable in the curvature of the projected field lines between the layers, due to the higher magnetic screening power of the superconducting regions. Such differences, however, are hardly detectable in the out-of-focus images due to the feature-broadening effect typical of the Fresnel technique.[25]

The differences between the two models are even less appreciable in the case of a pancake vortices stack pinned at large angles to some columnar defects. A 75° tilted stack of pancake vortices, aligned to a row of pinning centers piercing the specimen at the same angle, is reported in Fig. 3.

Whereas the relative distance between the dots is not influential on the phase maps, it is possible to appreciate the artifacts introduced by the small number of layers when the phase shift is calculated for a specimen tilted at α=30°. Figure 4(a) reports the holographic contour map 32× amplified and the out-of-focus image calculated for seven layers, a stack tilt angle of 85° and three values of the defocus parameter. It can be seen that both in the contour line map and in the out-of-focus images, especially at the lowest defocus value Z=300 mm (c), the single pancakes can be clearly distinguished.

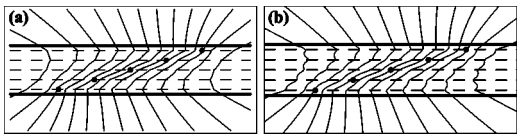

FIG. 3. Contour line plots representing the phase shift along y_S calculated with the pancake (a) and semicontinuous (b) models (n_L=5 layers). The contour lines represent phase shifts of 200 mrad. Simulation parameters, tilt angle of the stack of pancakes θ=75°, plot region 2×1 μm, specimen thickness t=400 nm and λ =200 nm. The dots mark the positions of the pancake vortices.

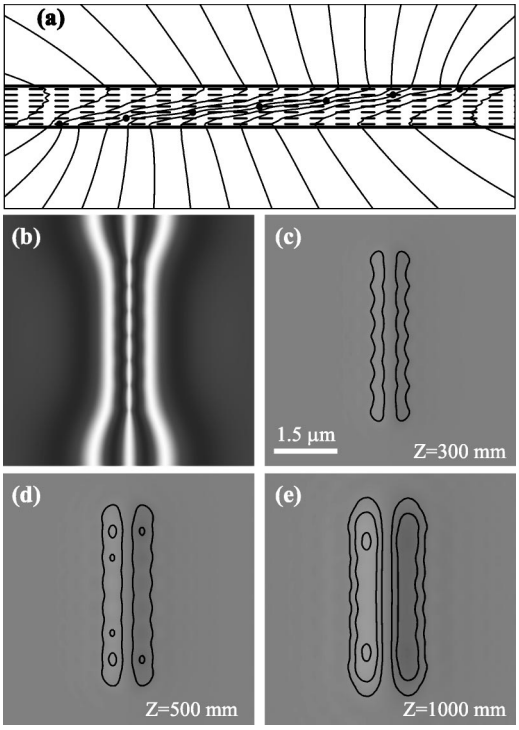

FIG. 4. (a) Phase contour line plot over a region of 5×2 μm, where each contour line represents a phase variation of $\pi/16$; (b) holographic contour maps $32\times$ amplified; (c)–(e) out-of-focus images. The image size in (b)–(e) is 6 μm. Simulation parameters, stack tilt angle $\theta=85°$, specimen tilt $\alpha=30°$, specimen rotation $\beta=0°$, number of layers $n_L=7$, specimen thickness $t=400$ nm, $\lambda=200$ nm. Each contour line superimposed to the out-of-focus images represents a contrast variation of 3%.

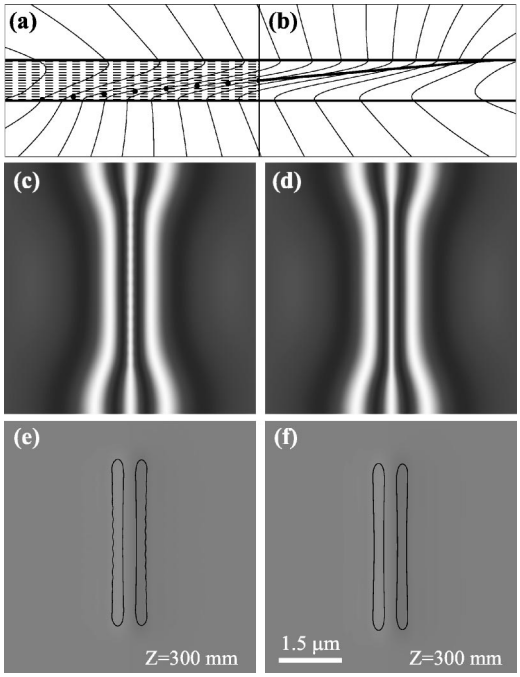

FIG. 5. Comparison between the semicontinuous (left column) and the continuous-anisotropic (right column) models. (a) and (b) Phase contour line plot over a region of 5×1.5 μm; (c) and (d) holographic contour maps $32\times$ amplified; (e) and (f) out-of-focus images (defocus value $Z=300$ mm). Simulation parameters, pancake stack/vortex core tilt angle $\theta=85°$, specimen tilt and rotation $\alpha=30°$, $\beta=0°$, number of layers $n_L=15$, specimen thickness 400 nm, anisotropy factor $\gamma=200$, $\lambda=200$ nm. Each contour line superimposed to the out-of-focus images represents a contrast variation of 3%.

If we increase the number of pancakes to 15, something possible only if the semicontinuous model is adopted, this artifact becomes undetetectable and the calculated image is undistinguishable from the one calculated by the continuous anisotropic model,[14] as shown in Fig. 5. This example clearly shows the usefulness of the new approach in order to avoid this kind of artifacts.

V. EXPERIMENTAL RESULTS

Let us briefly recall some of the experimental results reported in the paper by Tonomura *et al.*,[15] whose main purpose was to investigate the formation mechanism of unconventional arrangements of vortices in high-T_c superconducting thin films with an inclined applied magnetic field with respect to the layer plane. The observations were carried out by means of the Lorentz-Fresnel (out-of-focus) method in the newly developed 1 MV electron microscope,[11] equipped with a special magnetic stage able to provide applied fields up to 10 mT with an arbitrary direction.

Film samples, 300–400 nm thick, of single-crystalline YBCO ($T_c=92$ K) were prepared by thinning a region 30 μm$\times$100 μm, of a YBCO single crystal with a focused ion beam machine (Hitachi FB-2000). These samples, whose surfaces were parallel to the *ab* plane, were tilted around the *y* axis of 30° whereas the electron beam was incident along the optical axis *z*. A magnetic field of 0–10 mT was applied obliquely to the surface of the samples at incidence angles θ_H of 70°–90°, and vortices in arrangements reflecting the anisotropic layered structure of the materials were observed as Lorentz micrographs. The experimental results, taken at a defocus of 300 mm and at a temperature of 30 K are shown in Fig. 6, reproduced at large magnification so that contrast features of each single vortices are better visible. The angle between the magnetic field and the surface normal was varied between $\theta_H=75°$ and $\theta_H=85°$.

We note that each vortex has a circular shape for $\theta_H\leqslant75°$, as shown in Fig. 6(a), and gradually elongates in the direction of the field when the angle is above 80°, as shown in Fig. 6(b), where the field was applied at $\theta_H=82°$. At slightly higher angles, the shape changes dramatically, becoming dumbbell-like [Fig. 6(c), $\theta_H=83°$] and even somewhat splitted in some cases, as emphasized by white arrows in Fig. 6(d), where $\theta_H=84°$. For the largest angle, $\theta_H=85°$, the vortices appear very elongated, with low contrast. At least one of them, indicated by an arrow in (e), show a clear contrast splitting.

It will be shown in the following that this behavior cannot be reproduced by simulations computed assuming a straight vortex core (or aligned stack in the layered models). In fact, for straight configurations such as those previously reported, the vortex should appear more elongated than observed, and

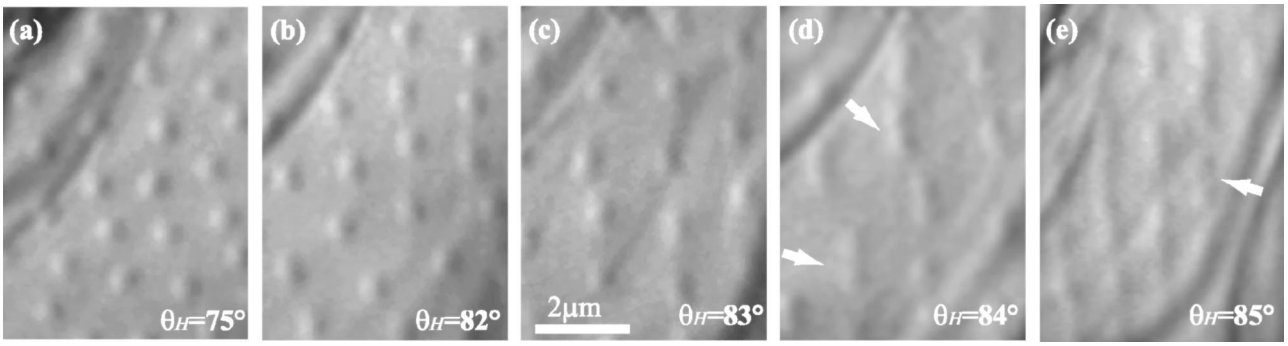

FIG. 6. Lorentz micrographs of vortices in YBCO film sample at tilted magnetic fields ($T=30$ K, $|\mathbf{H}_{app}|=0.3$ mT, angles indicated in the figure). When the tilt angle becomes larger than 80°, the vortex images start elongating (b) and (c). For the applied field angle of 84° we observe dumbbell features, and apparent splitting of the vortex contrast, as indicated by white arrows in (d). For the largest angle, 85°, vortices appear very elongated, with remaining indication of stack splitting.

no dumbbell-like or splitted contrast features are ever present. This discrepancy prompted us to consider more complicated distributions of pancake vortices on the layers, something possible only within the framework of the semicontinuous model.

VI. INTERPRETATION OF THE EXPERIMENTAL RESULTS

The theoretical framework for interpreting our results has not been thoroughly investigated in literature, where only the cases of very thin film ($t \ll \lambda$) and of a thick slab ($t \gg \lambda$) have been considered.[26,27] These results show that in thin films the vortex lines are nearly straight and perpendicular to the surface, whereas in thick slabs each vortex is directed near the surface along the normal to the surface itself and inside is aligned with the applied field.

The experimental results of Sec. V correspond to the intermediate case $t=2\lambda$, so that for their simulation we followed two complementary approaches. First we consider an aligned stack of pancake vortices tilted at various angles, thus having a shorter projected length. Figure 7 reports simulations computed with the anisotropic model, owing to the similarity of results with the semicontinuous one demonstrated in Fig. 5. The first line reports the phase contour plot, with the core evidenced by a bold line, followed by the holographic contour maps (second line) and the out-of-focus images at $Z=300$ mm, third line. All these data have been calculated for the high anisotropic case $\gamma=200$ (the parameter γ is defined as the ratio between the penetration depths along the *c*-axis and the *ab* plane, i.e., $\gamma=\lambda_c/\lambda_{ab}$),[14] while the last line reports the out-of-focus images at $Z=300$ mm for $\gamma=5$, a value which better correspond to the investigated material (YBCO). It can be ascertained that the out-of-focus

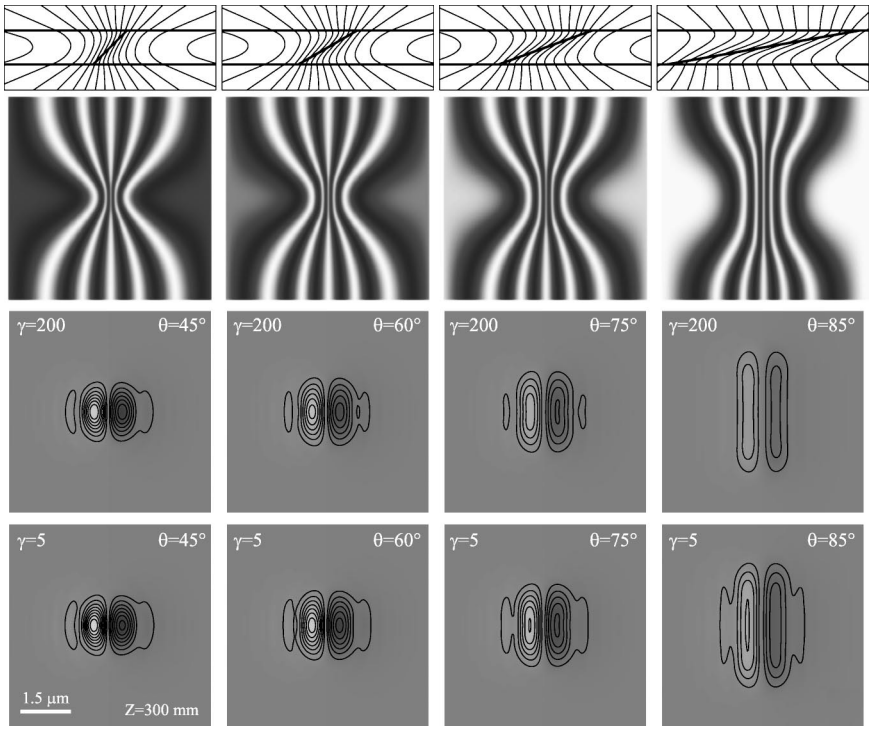

FIG. 7. Simulation series for increasing core tilt angles from left to right, $\theta=45°$, 60°, 70°, 80°. From top to bottom, phase contour line plot over a region of 2.5 $\times 1$ μm, where each contour line represents a phase variation of $\pi/16$; holographic cosine map, 32× amplified; out-of-focus image for $\gamma=200$; out-of-focus image for $\gamma=5$. Simulation parameters, specimen tilt and rotation $\alpha=30°$, $\beta=0°$, core tilt angle θ indicated in each figure, specimen thickness 400 nm, $\lambda=200$ nm, defocus distance $Z=300$ mm. Each contour line superimposed to the out-of-focus images represents a contrast variation of 3%.

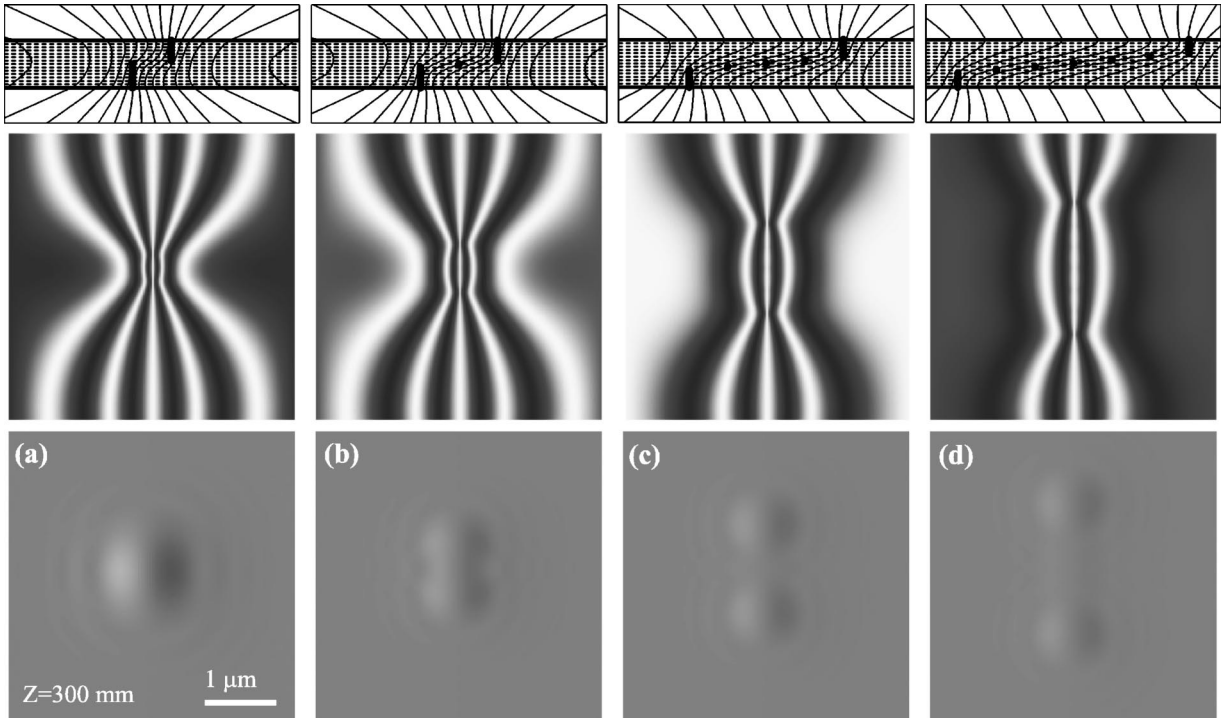

FIG. 8. Simulation series for exotic (kinked) core structures, where the pancakes are distributed according to the dots in the phase contour line plots. From top to bottom, phase contour line plot over a region of 2.5×1 μm, where each contour line represents a phase variation of $\pi/16$; holographic cosine map, $32\times$ amplified; out-of-focus images with $Z=300$ mm. Simulation parameters, specimen tilt and rotation $\alpha=30°$, $\beta=0°$, specimen thickness 400 nm, number of layers $n_L=15$, $\lambda=200$ nm.

images for different γ differ only by a variation of the contrast (higher for lower γ) but have the same appearance, in particular the same projected fluxon length and do not display any dumbbell-like feature.

We have then considered the thick slab case result. The complicated core structures analyzed in Refs. 17 and 18, have been modeled by considering a core aligned with the field in the interior of the specimen, at an angle of 85°, and kinked near the surfaces and aligned perpendicularly to them. As remarked before, this fluxon core structure can be analyzed only within the realm of the semicontinuous model. The results are shown in Fig. 8, where the kinked structure has been chosen in such a way that the fluxon has the same projected fluxon length as in Fig. 7.

The comparison between Figs. 7 and 8 shows that the out-of-focus image of the kinked structure presents a dumbbell-like feature, where the stack of pancake appears to be divided into two. The separation is not visible in (a), while the two half-stacks are progressively more separated in (b)–(d). These simulations show a better agreement with Fig. 6 than those reported in Fig. 7.

Finally, we may wonder about the seemingly rather abrupt transition from an elongated to a dumbbell contrast occuring at about 82°. Considering that the inner part of the vortex is almost negligible, and that the net result is the transition from a straight to a kinked vortex structure, we note the similarity of this behaviour with the instability of a tilted vortex line investigated by Benkraouda and Clem.[28] They found that for a stack of electromagnetically coupled two-dimensional pancake vortices the line tension become negative at an angle of ~52°, so that a kinked structure is energetically favored. The difference between the angle values may be attributed to a stronger Josephson coupling between the layers and, perhaps, to the effect of the surfaces and finite specimen thickness, two factors not taken into account in the theoretical analysis.

VII. CONCLUSIONS

In this work we have improved the layered model for superconducting vortices in high-T_c materials. The number of layers where to locate pancake vortices has been increased considerably. With the new semicontinuous models, the simulation artifacts due to the small number of layers have been removed. Moreover, the analysis of more exotic structures can be implemented in order to improve image interpretation of experimental results. In particular it has been shown that the shorter projected length of the fluxon visible in the experiments can be attributed to a kinked structure of the core, whose characteristic feature is a dumbbell-like contrast in the out-of-focus image for large applied field angles. As our experiments are in a thickness range not yet theoretically investigated we hope to stimulate work in this direction. The unique opportunity offered by transmission electron microscopy to observe directly vortices in superconductors will hopefully result in a better understanding of the core structure as related to applied field and material properties.

ACKNOWLEDGMENTS

The authors thank N. Osakabe, J. Endo, O. Kamimura, T. Onogi, and R. Sugano (Hitachi, Ltd.) for discussions and

valuable comments; Y. Shiohara (ISTEC), T. Matsumoto, K. Takagi, and T. Fukazawa (Hitachi, Ltd.) for sample preparation; T. Kanemura and T. Shimotsu (Hitachi Science Systems, Ltd.) for assistance in operating the focused ion beam machine; N. Moriya (Hitachi, Ltd.), for technical assistance in the experiment. This work was partially supported by New Energy and Industrial Technology Development Organization (NEDO) as Collaborative Research and Development of Fundamental Technologies for Superconductivity Applications.

[1] K. Harada, T. Matsuda, J.E. Bonevich, M. Igarashi, S. Kondo, G. Pozzi, U. Kawabe, and A. Tonomura, Nature (London) **360**, 51 (1992).
[2] J.E. Bonevich, K. Harada, T. Matsuda, H. Kasai, T. Yoshida, G. Pozzi, and A. Tonomura, Phys. Rev. Lett. **70**, 2952 (1993).
[3] P.L. Gammel, C.A. Duran, D.J Bishop, V.G. Kogan, M. Ledvij, A.Yu. Simonov, J.P. Rice, and D.M. Ginsberg, Phys. Rev. Lett. **69**, 3808 (1992).
[4] H.F. Hess, R.B. Robinson, R.C. Dynes, J.M. Valles, and J.V. Waszczak, Phys. Rev. Lett. **62**, 214 (1989).
[5] R. Straub, S. Keil, R. Kleiner, and D. Koelle, Appl. Phys. Lett. **78**, 3645 (2001).
[6] A. Grigorenko, S. Bending, T. Tamegai, S. Ooi, and M. Henini, Nature (London) **414**, 728 (2001).
[7] L.N. Vu, M.S. Wistrom, and D.J. Van Harlingen, Appl. Phys. Lett. **63**, 1693 (1993).
[8] P.E. Goa, H. Hauglin, M. Baziljevich, E. Il'yashenko, P.L. Gammel, and T.H. Johansen, Supercond. Sci. Technol. **14**, 729 (2001).
[9] M.R. Eskildsen, M. Kugler, S. Tanaka, J. Jun, S.M. Kazakov, J. Karpinski, and O. Fischer, Phys. Rev. Lett. **89**, 187003 (2002).
[10] A. Moser, H.J. Hug, I. Parashikov, B. Stiefel, O. Fritz, H. Thomas, A. Baratoff, H.J. Güntherodt, and P. Chaudhari, Phys. Rev. Lett. **74**, 1847 (1995).
[11] T. Kawasaki, T. Yoshida, T. Matsuda, N. Osakabe, A. Tonomura, I. Matsui, and K. Kitazawa, Appl. Phys. Lett. **76**, 1342 (2000).
[12] A. Tonomura, H. Kasai, O. Kamimura, T. Matsuda, K. Harada, Y. Nakayama, J. Shimoyama, K. Kishio, T. Hanaguri, K. Kitazawa, M. Sasase, and S. Okayasu, Nature (London) **412**, 620 (2001).
[13] O. Kamimura, H. Kasai, T. Akashi, T. Matsuda, K. Harada, J. Masuko, T. Yoshida, N. Osakabe, A. Tonomura, M. Beleggia, G. Pozzi, J. Shimoyama, K. Kishio, T. Hanaguri, K. Kitazawa, M. Sasase, and S. Okayasu, J. Phys. Soc. Jpn. **71**, 1840 (2002).
[14] M. Beleggia, G. Pozzi, J. Masuko, N. Osakabe, K. Harada, T. Yoshida, O. Kamimura, H. Kasai, T. Matsuda, and A. Tonomura, Phys. Rev. B **66**, 174518 (2002).
[15] A. Tonomura, H. Kasai, O. Kamimura, T. Matsuda, K. Harada, T. Yoshida, T. Akashi, J. Shimoyama, K. Kishio, T. Hanaguri, K. Kitazawa, T. Masui, S. Tajima, N. Koshizuka, P.L. Gammel, D. Bishop, M. Sasase, and S. Okayasu, Phys. Rev. Lett. **88**, 237001 (2002).
[16] J.R. Clem, Phys. Rev. B **43**, 7837 (1991).
[17] J.R. Clem, Physica C **235-240**, 2607 (1994).
[18] M.W. Coffey and E.T. Phipps, Phys. Rev. B **53**, 389 (1996).
[19] M. Beleggia and G. Pozzi, J. Electron Microsc. **51**, S73 (2002).
[20] J. Pearl, Appl. Phys. Lett. **5**, 65 (1964).
[21] M. Beleggia and G. Pozzi, Phys. Rev. B **63**, 054507 (2001).
[22] A. Fukuhara, K. Shinagawa, A. Tonomura, and H. Fujiwara, Phys. Rev. B **27**, 1839 (1983).
[23] G. Pozzi, Adv. Imaging Electron Phys. **93**, 173 (1995).
[24] J.E. Bonevich, K. Harada, H. Kasai, T. Matsuda, T. Yoshida, G. Pozzi, and A. Tonomura, Phys. Rev. B **49**, 6800 (1994).
[25] M. Beleggia, G. Pozzi, and A. Tonomura, J. Magn. Magn. Mater. **272-276**, E143 (2004).
[26] E.H. Brandt, Phys. Rev. B **48**, 6699 (1993).
[27] A. Yu. Martynovich, J. Exp. Theor. Phys. **78**, 489 (1994).
[28] M. Benkraouda and J.R. Clem, Phys. Rev. B **53**, 438 (1996).